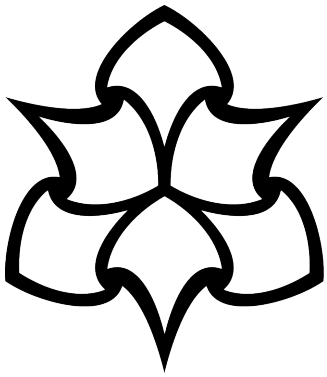

# Precious Metal-Free Nickel Nitride Catalyst for the Oxygen Reduction Reaction

Authors: Melissa E. Kreider[1], Alessandro Gallo[1,2], Seoin Back[1,3], Yunzhi Liu[4], Samira Siahrostami[1,6], Dennis Nordlund[5], Robert Sinclair[4], Jens K. Norskov,[1,2,7] Laurie A. King[1], Thomas F. Jaramillo[1,2]

Affiliations:
[1] Department of Chemical Engineering, Stanford University, 443 Via Ortega, Stanford, California 94305, United States
[2] SUNCAT Center for Interface Science and Catalysis, SLAC National Accelerator Laboratory, 2575 Sand Hill Road, Menlo Park, California 94025, United States
[3] Department of Chemical Engineering, Carnegie Mellon University, Pittsburgh, Pennsylvania 15213, United States
[4] Department of Materials Science and Engineering, Stanford University, 496 Lomita Mall, Stanford, California 94305, United States
[5] Stanford Synchrotron Radiation Lightsource, SLAC National Accelerator Laboratory, 2575 Sand Hill Road, Menlo Park, California 94025, United States
[6] Department of Chemistry, University of Calgary, 2500 University Drive NW, Calgary, Alberta, Canada T2N 1N4
[7] Technical University of Denmark, DK-2800 Lyngby, Denmark

Corresponding authors:
Laurie A. King email: lking10@stanford.edu
Thomas F. Jaramillo email: jaramillo@stanford.edu

Abstract:

With promising activity and stability for the oxygen reduction reaction (ORR), transition metal (TM) nitrides are an interesting class of non-platinum group catalysts for polymer electrolyte membrane fuel cells (PEMFCs). Here we report an active thin film nickel nitride catalyst synthesized through a reactive sputtering method. In RDE testing in 0.1M $HClO_4$ electrolyte, the crystalline nickel nitride film achieved high ORR activity and selectivity to 4 electron ORR. It also exhibited good stability during 10 h and 40 h chronoamperometry (CA) measurements in acid and alkaline, respectively. A combined experiment-theory approach, with detailed *ex-situ* characterization with TEM and NEXAFS to reveal a mixed $Ni_4N/Ni_3N$ structure with an amorphous surface oxide and DFT calculations to provide insight into the surface structure during catalysis, is highlighted. Design strategies for activity and stability improvement through alloying and nanostructuring are discussed.

Keywords:

Electrocatalysis, oxygen reduction reaction, non-precious metal catalysts, transition metal nitrides, reactive sputter deposition, density functional theory

## Introduction

Proton-exchange membrane fuel cells (PEMFCs) are a promising technology towards enabling efficient and clean electricity production for transportation and industrial applications. In a PEMFC, hydrogen fuel is oxidized at the anode and oxygen is reduced at the cathode, generating electricity and releasing water as a benign by-product. Current commercial PEMFCs utilize expensive platinum-based catalysts for both the anode and cathode.[1] In particular, prohibitively large Pt loadings are required at the cathode to overcome the sluggish kinetics of the oxygen reduction reaction (ORR).[2,3] While much work has focused on improving the mass activity of Pt ORR catalysts,[4–7] limitations, including scarcity, instability, and susceptibility to carbon monoxide poisoning, remain.[8–10] Therefore, the discovery of earth abundant, non-precious metal ORR catalysts is of critical interest for the large scale implementation of fuel cell technology.

Many non-platinum group (non-PGM) materials have been explored for ORR, including transition metal oxide[11,12] and nitrogen-doped carbon[13] catalysts that have shown promising activity in alkaline electrolyte, and metal-nitrogen-carbon[14–16] catalysts that have achieved Pt-like activity in acid. Another promising class of earth-abundant materials are the transition metal nitrides, which are electronically conductive and have shown enhanced catalytic activity relative to their parent metal due to beneficial changes in the d-band structure.[17] Moreover, nitrides have achieved activity approaching that of the noble metals for a variety of reactions.[18] ORR activity has been demonstrated for several nitrides, including Co, Fe, and Ti.[19–24] Nitrides of Mo and W have also shown promising stability in acidic electrolyte due to their high corrosion resistance.[25–27] Particular interest has focused on the bimetallic nitride $Co_{0.6}Mo_{1.4}N_2$, which combines the activity of $Co_xN$ with the acid stability of $Mo_xN$.[28–30]

Nickel-based nitride catalysts have also shown some ORR activity. Specifically, a high surface area $Ni_3N$ on Ni-foam catalyst demonstrated low overpotential and good stability for HER and OER, as well as preliminary evidence of activity for ORR in alkaline media.[31] $Ni_3FeN$ nanostructures have shown promising bifunctional activity, both as supports and catalysts, for metal-air batteries in alkaline media.[32–34] Additionally, $Ni_3N$ quantum dots supported on NiO nanosheets have shown good activity and stability for ORR in alkaline.[35] Herein, we demonstrate an ORR active nickel nitride catalyst in acid for the first time. Through extensive electrochemical, materials, and theoretical characterization of a well-defined, carbon-free thin film catalyst, we investigate the fundamental ORR activity, selectivity, and stability of nickel nitride in both acidic and alkaline electrolyte. DFT is utilized to construct Pourbaix diagrams and identify the active surface of the catalyst.

## Materials and Methods

### Materials

Glassy carbon electrodes (Pine Research Instrument, 0.196 $cm^2$ geometrical area), graphite counter electrode, platinum wire, silicon wafers (WRS, 100 mm, P/Bor <100>, 10-20 Ohm-cm), Ni sputtering target (Kurt J Lesker, 99.99% purity, 2" diameter), Ti sputtering target (Kurt J Lesker, 99.99% purity, 2" diameter), perchloric acid (Honeywell Fluka, 70%), potassium hydroxide (Fisher Chemical, 86.4% assay), were all used as received and without further purification unless otherwise stated.

### Synthesis

Nickel nitride thin films were prepared by DC reactive sputtering using a Lesker Sputter. Prior to the nitride synthesis, a 20 nm thick Ti sticking layer was synthesized by sputter deposition (3 minutes, 200W, 100% Ar, 3 mTorr) onto the polished glassy carbon disk electrode. Subsequently, without breaking vacuum, the Ni target was sputtered in a mixture of 75% Ar, 25% $N_2$ plasma to deposit ~130 nm of $Ni_xN$. The magnetron power supply was maintained at 200 W and the chamber pressure was 8 mTorr. The substrate was held at 180 ± 10 ˚C with a substrate bias of 100 V throughout the deposition. The $Ni_3N$ and $Ni_4N$ standards used for near edge X-ray absorption fine structure (NEXAFS) spectroscopy were synthesized on silicon substrates; $Ni_3N$ was made by increasing chamber pressure to 18 mTorr, while $Ni_4N$ was made by decreasing the substrate temperature to 90 ˚C. Ni and NiO thin films were synthesized using the same conditions, but with 100% Ar and 20% $O_2$ & 80% Ar plasma, respectively. Films were also synthesized on Si wafers, with native $SiO_2$ layer, for structural characterization.

### Physical characterization

Grazing-incidence X-ray diffraction (XRD) data were obtained using a D8 Venture single crystal diffractometer (Bruker, λ=1.5418 Å) at an incidence angle of 5˚. Top-down and cross-sectional scanning electron microscopy (SEM) was conducted with a FEI Magellan 400 XHR SEM. X-ray photoelectron spectroscopy (XPS) was performed with a Phi Versaprobe 1 using monochromatized Al Kα (1486 eV) radiation. All XPS spectra were calibrated to the C 1s peak at a binding energy of 284.8 eV. CasaXPS software was used to perform peak fitting with Shirley backgrounds.

The cross-section TEM specimen was prepared conventionally.[36] The samples were glued and mechanically grounded to approximately 15 μm in thickness. The cross-section specimen was further ion milled until electron transparent in a Gatan PIPS II ion milling machine. Argon ion beams with 5 keV energy were induced at an incident angle of 5 degrees to create a hole at the center of the specimen. After the formation of the hole,

the beam energy was gradually reduced to 0.5 keV for final cleaning. TEM experiments were conducted in a FEI Titan 80-300 environmental transmission electron microscope equipped with a spherical aberration corrector in the image-forming (objective) lens. Selected Area Diffraction Patterns (SADP) were calibrated using a standard Si [110] diffraction pattern taken under the same conditions.

NEXAFS data for N and O K-edge and Ni L-edge were collected at the Stanford Synchrotron Radiation Light Source (SSRL) on BL 8-2 and 10-1 in total fluorescence yield (TFY) and total electron yield (TEY) modes, operating the monochromator with 0.2 eV (for N and O K-edges) and 0.3 eV (for Ni L-edge) resolution, respectively. NiO, $Ni_3N$, and $Ni_4N$ were used as standards. The collected data were normalized to the edge jump after subtraction of the pre-edge region. TFY enables bulk sensitivity with a penetration depth on the order of 100 nm, while TEY has a penetration depth of 5-10 nm.

NEXAFS simulations for the N K-edge were conducted with OCEAN code[37,38] and FEFF 9 code[39] using a broadening of 1.0 eV and 0.52 eV, respectively, and the crystallographic structures of $Ni_4N$ and $Ni_3N$. O K-edge was simulated with the FEFF 9 code using a SCF cluster of 6 Å and increasing the radius of the FMS cluster from 3 Å to 9 Å starting from the crystallographic structure of NiO. A broadening of 0.8 eV was applied to simulate the experimental broadening (primarily instrumental, core-hole, and vibrational broadening). The screening of the core-hole was computed using random phase approximation (RPA) and the H-L self-energy was used for the calculation of the exchange correlation potential.

## Electrochemical Testing

Electrochemistry was performed using a rotating disk electrode (Pine Research Instrument) in a three-electrode glass cell, with 0.1 M $HClO_4$ or 0.1 M KOH electrolyte purged with oxygen or nitrogen. An in-house built reversible hydrogen electrode (RHE) was used as the reference electrode and a graphite rod as the counter electrode. The series resistance of the cell was measured at 100 kHz and the iR losses were compensated at 85%. The remaining 15% was corrected after testing. Electrochemical activity was assessed using cyclic voltammetry (CV), sweeping reversibly from 0.8 V to 0.05 V at a scan rate of 20 mV/s using a Biologic VSP-300 Potentiostat. Unless otherwise stated, the oxygen purged voltammograms were corrected for background current by subtracting the baseline (nitrogen) sweep. For simplicity, only cathodic CV sweeps are shown in the main text; full CVs are shown in the SI. Stability was evaluated using chronoamperometry, holding at a constant potential of 0.15 V. Selectivity measurements were conducted using a rotating ring disk electrode (Pine Research Instrument) with a Pt ring held at 1.2 V vs RHE to measure the $H_2O_2$ produced in the reaction. See the SI for details of ring calibration and selectivity calculations.

## Computational Details

We performed density functional theory (DFT) calculations using the Vienna Ab Initio Simulation Package (VASP)[40,41] with the PBE exchange-correlation functional[42] and projector augmented-wave (PAW) pseudopotentials.[43] We added a Hubbard-U correction (PBE+U)[44] on insulating Ni oxide materials to include the on-site Coulomb interaction of localized electrons. The value of the Hubbard interaction, U, for Ni was chosen to be 6.2 eV in accordance with the literature.[45,46] The energy cutoff, convergence criteria for self-consistent iterations, and for geometry relaxation were set to 500 eV, $10^{-4}$ eV, 0.05 eV/Å, respectively. Further computational details can be found in the SI.

## Results and Discussion

### Characterization

The reactively sputtered nickel nitride films are ~160 nm in thickness as shown by cross-sectional scanning electron microscopy (SEM) in Figure 1A. The film consists of well-defined nanopillars, which are variable in height but closely packed to form a rough, dense film. The 20-30 nm Ti sticking layer is visible beneath the pillars. The top down SEM in Figure 1B shows that the nanopillars are pyramids with either square or triangular base shapes. The larger square prisms have an average diameter (distance from opposite corners, viewed from above) of 70 nm, while the triangular prisms are 30-40 nm.

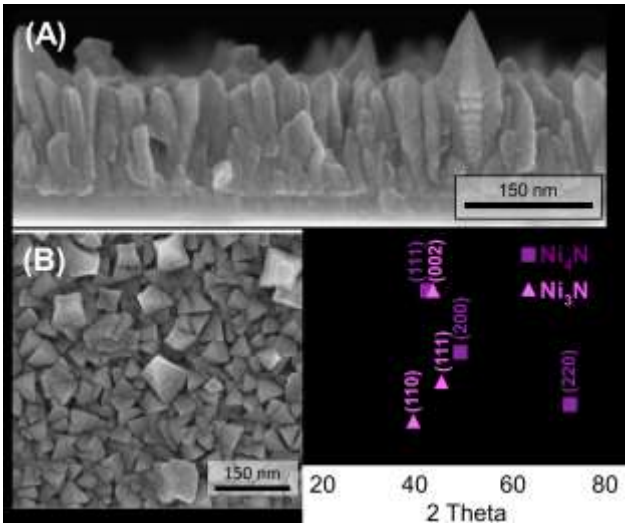


**Figure 1.** Characterization of as-prepared, sputtered $Ni_xN$ thin films. (A) Cross-sectional and (B) top down SEM micrographs, (C) XRD pattern with ICDD references and corresponding crystal planes.

X-ray diffraction (XRD) of the thin films shows peaks corresponding to both hexagonal $Ni_3N$ (ICDD 00-010-0280 at 2Θ of 39.9˚, 42.7˚, and 45.2˚) and cubic $Ni_4N$ (ICDD 00-036-1300 at 42.0˚, 49.3˚, and 72.0˚), confirming that no other crystalline species are present (Figure 1C).

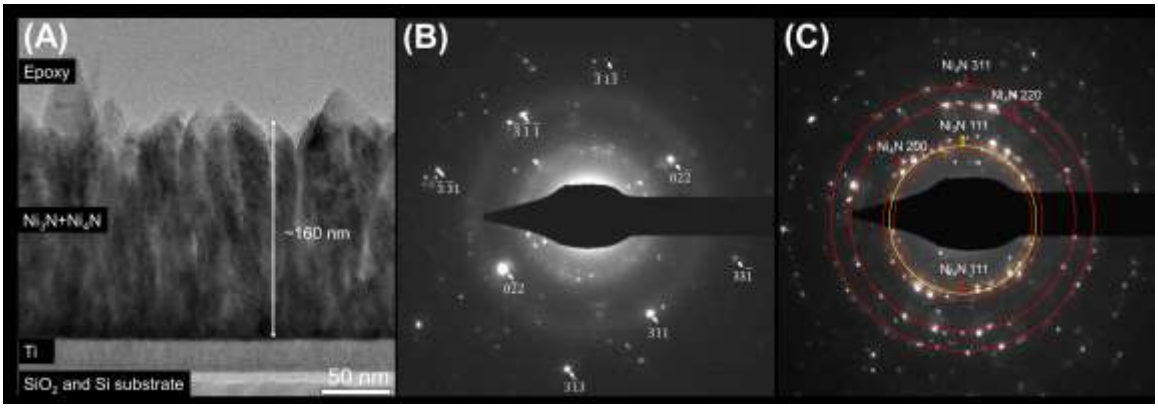


**Figure 2.** TEM-SADP (selected area diffraction pattern) characterization of as-prepared $Ni_xN$ thin films. (A) Cross-sectional view, (B) SADP taken from top surface of the film matching diffraction pattern of $Ni_4N$ from $[\bar{2}33]$ zone axis, (C) SADP taken from the bulk region of the film showing diffraction rings of $Ni_4N$ and $Ni_3N$.

The films were also analyzed using cross-sectional transmission electron microscopy (TEM). The TEM image of the film in Figure 2A shows a pillar morphology, as seen in SEM, as well as discrete titanium (20 nm thick), silicon dioxide (7 nm thick), and silicon layers. Distinct crystalline regions are also visible (Fig. S1). Selected area diffraction patterns (SADP) were used to determine the crystal structures at the surface and in the bulk, as shown in Figure 2B and C, respectively. The selected area aperture positions are shown in Figure S2. In Figure 2B, the diffraction pattern measured at the surface matches the $Ni_4N$ cubic structure. The measured d-spacings of diffraction spots along the two orthogonal directions are 0.131 nm and 0.111 nm. These match well with the $(0\bar{2}2)$ and $(311)$ planes of the reference $Ni_4N$. These also suggest that the diffraction pattern was taken near a $[\bar{2}33]$ zone axis of $Ni_4N$. The diffraction pattern from the bulk region shows diffraction rings (labeled in red) of $Ni_4N$ which correspond to the (111), (200), (220), and (311) planes. This indicates that the bulk of the thin film is polycrystalline. An additional ring (labeled in yellow) was observed between the (111) and (200) rings of $Ni_4N$. The d-spacing of this ring matches the (111) plane spacing of $Ni_3N$. The SADP indicates that the film is primarily composed of $Ni_4N$, with a minor phase of $Ni_3N$ in the bulk. However, it is important to note that the analyzed volume of our polycrystalline film from this method is limited. To probe a broader region of the sample, we employed NEXAFS spectroscopy, as discussed in the next section.

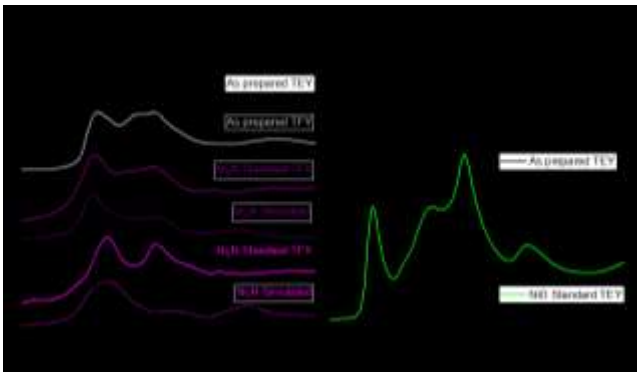

**Figure 3.** NEXAFS spectra of as-prepared, sputtered $Ni_xN$ thin films. (A) N K-edge of the sample, $Ni_3N$ and $Ni_4N$ standards, and simulated spectra; (B) O K-edge of the sample and NiO standard. Dashed lines are intended as guides for the reader. TEY: surface; TFY: bulk.

To further probe the structure and chemical state of the catalyst, the films were characterized using NEXAFS spectroscopy. In Figure 3A, the N K-edge NEXAFS spectra for the as-prepared catalyst are compared with experimental and simulated spectra for $Ni_3N$ and $Ni_4N$ standards. The spectra were collected in TEY and TFY modes, allowing for a comparison between the surface (TEY: few nm) and the bulk of the film (TFY). Two main peaks are present both for the surface and the bulk of the as-prepared sample, though differences are evident between the two spectra. For TEY, the feature at 397.5 eV matches well with both the experimental and simulated spectrum of $Ni_4N$. The TFY signal shows a shift of the peak at 397.5 eV towards higher energy and the appearance of a shoulder corresponding to $Ni_3N$. We can thus confirm that the catalyst is a mixture of $Ni_4N$ and $Ni_3N$, as indicated by XRD and TEM analyses, and locate $Ni_3N$ in the bulk. The feature at 400.5 eV is associated with the oxidation of the surface of the nitride film upon exposure to air after synthesis, as has been previously reported for other transition metal nitrides.[47,48] Notably, the fact that the intensity of this feature considerably decreases in the bulk of the material provides evidence for the presence of a surface N state different than in the pure bulk nitride film. This is also observed in the experimental spectra for the $Ni_4N$ and $Ni_3N$ standards (Figure S3).

Figure 3B shows experimental O K-edge spectra for the catalyst and the NiO standard, which allow for further characterization of surface oxidation. The TFY signal for O was negligible, confirming that the oxidation process is limited to the surface and there is no oxygen incorporation in the bulk. The signal for the oxidized layer on top of the nitride film consists of a peak at 532.8 eV, shifted to higher energy compared to the bulk NiO, and a broad feature at 540.5 eV, which has been reported for small native Ni oxide clusters on top of Ni films.[49] It was concluded that none of the defined features typical of crystalline NiO were detected due to the amorphous nature of the small NiO domains. O K-edge spectra for NiO clusters of various dimensions were simulated (Fig. S4). The simulated

spectrum for a NiO cluster with ca. 5 Å radius (57 atom cluster) is the best match to the experimental, suggesting the presence of these clusters on the nitride surface. The Ni L3- and L2-edge spectra also support the presence of oxidized $Ni_4N$ on top of $Ni_3N$ (Fig. S5). Our spectroscopic measurements thus indicate that prior to testing, the catalyst structure consists of small clusters of NiO on top of $Ni_4N$, with $Ni_3N$ crystallites also present in the bulk.

## Electrochemistry

The ORR activity and selectivity of the nickel nitride catalyst was assessed using a rotating ring disk electrode (RRDE) in both acidic (0.1 M perchloric acid) and alkaline (0.1 M potassium hydroxide) electrolyte. Figure 4A shows the activity and selectivity of the synthesized catalyst, with the ORR polarization curve measured on the disk electrode (solid lines) and the $H_2O_2$ oxidation current measured on the platinum ring electrode (dashed lines). Comparison with the activity of a commercial Pt/C (46.6% from TKK) catalyst is shown in Figure S6.[50] In acid, the ORR onsets (defined as the potential required to reach 100 μA/cm$^2$ geometric current density) at 0.68 V vs RHE and reaches the mass transport limited current density of 6.1 mA/cm$^2$ at 0.2 V vs RHE. Furthermore, the halfwave potential is 0.49 V vs RHE, indicating a relatively sharp onset. This is promising activity for a non-Pt group metal catalyst in acid and is comparable to the metal nitrides currently reported in the literature (Table S3).[51–53] Nickel nitrogen-doped carbon (Ni-NC) type catalysts have also demonstrated good ORR performance, but they cannot be directly compared with this work due to their high surface area and the contributions of the NC support.[54,55] In alkaline electrolyte, nickel nitride shows similar activity with an onset at 0.68 V vs RHE but has a lower mass transport limited current density of 4 mA/cm$^2$, as well as a slower onset with a halfwave potential of 0.42 V vs RHE. This difference in activity is reflected in the Tafel slopes: 89.7 mV/decade in acid compared to 175 mV/decade in alkaline (Fig. S7). Similar pH dependent Tafel slope trends have been reported in the literature.[56] Aside from the Tafel slopes, PGM-free catalysts are generally more ORR active in alkaline, with higher onset and halfwave potentials (Table S3). The reversal in that trend for this nickel nitride system can likely be attributed to different $H_2O_2$ selectivity and different surface structures under reaction conditions, which will be discussed in the following sections.

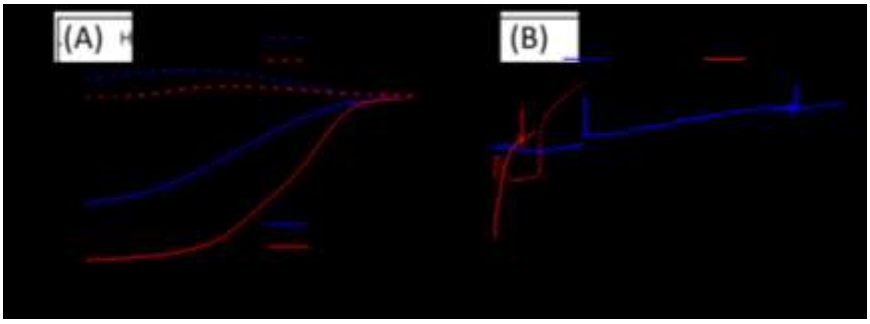


**Figure 4**. Electrochemical performance of $Ni_xN$ in acid (red) and base (blue). (A) RRDE measurements showing ORR polarization curves and $H_2O_2$ current density for nickel nitride. (B) Chronoamperometry (CA) profile at 0.15 V vs RHE in acid, for 2 samples tested under different cycling parameters, and in base.

For PEMFCs, high selectivity to the 4-election reduction, corresponding to a low $H_2O_2$ current, is preferred. In acid, the selectivity of the catalyst to $H_2O_2$ (2-electron reduction) was found to decrease with increasing overpotential and was negligible at potentials below 0.3 V vs RHE. (Fig. S10). The $H_2O_2$ current was used to calculate the electron transfer number, n, which was found to range from 3.2 (at 0.6 V vs RHE) to 4.0 (at 0.1 V vs RHE) (see SI for calculations). In alkaline electrolyte, nickel nitride has higher selectivity towards $H_2O_2$, with n values ranging from 2.4 at 0.6 V vs RHE up to 3.4 at 0.1 V vs RHE. This high selectivity to $H_2O_2$, as well as the onset of ORR activity close to the thermodynamic limiting potential of 0.70 V vs RHE for 2-electron ORR, indicates that in alkaline electrolyte the catalyst is unable to turnover 4-electron ORR until the onset of 2-electron ORR. This limitation to the thermodynamic potential of 2-electron ORR likely contributes to the lower activity in alkaline electrolyte.

In addition to activity and selectivity, stability is a crucial performance metric for any catalyst. Here, electrochemical stability was assessed using chronoamperometry, and the use of post-test characterization and theoretical calculations to evaluate chemical stability will be discussed in later sections. Figure 4B shows stability tests for nickel nitride in acid and alkaline electrolyte. After 3 CVs, catalyst stability was evaluated by chronoamperometry (CA) at 0.15 V vs RHE. CVs were run every 5 h to assess changes in activity (Fig. S11).

In alkaline, the catalyst improved over the first 5 h of the chronoamperometry hold, increasing from 3.3 to 3.5 $mA/cm^2$ of current density in the CA, and the CV after 5 h demonstrated improvement of 25 mV and 75 mV in onset and half-wave potential, respectively (Fig. S11B). Subsequent CVs show a slow degradation, with a loss of approximately 0.2 $mA/cm^2$ every 5 h from 10 h to 30 h. The noise in the data, observed at 3 h, is due to bubble formation on the surface of the catalyst. The bubble was removed mechanically and had no lasting effect on catalyst performance. All other spikes correspond to switching between the CA and CVs. The catalyst continued to degrade

slowly, with current density losses of 25% at 24 h and 40% at 40 h, at which time the stability test was ended.

Interestingly, in acid, the activity and stability of the nickel nitride catalyst was found to be dependent on the cycling parameters of the cyclic voltammogram (CV). To illustrate this dependence, Figure S12 shows cathodic sweeps, with no background subtraction, for two sibling catalysts in acid. The catalysts were tested identically, except that the sweeps started either at more positive (0.8 V vs RHE), as was shown in Figure 4A, or less positive (0.15 V vs RHE) potential. The “more positive start” catalyst shows superior activity, with both an earlier onset and larger limiting current density. However, it loses activity more rapidly, producing only 3 mA/cm$^2$ after 5 h, corresponding to a 50% loss in activity. CVs during the stability test for the “less positive start” catalyst are shown in Figure S11A, with relatively similar ORR activity at 0 and 5 h, but a significant loss of activity during the cycle at 10 h. These differences in activity and stability between these testing protocols, as well as the losses caused by the CVs during the CA, provide evidence that the catalyst is very sensitive to applied potential.

Sensitivity to potential is likely a consequence of surface oxidation reactions which occur in the ORR potential window.[57] In both $N_2$ and $O_2$ scans, there was an irreversible oxidative peak on the anodic sweep in the 0.65 – 0.8 V vs RHE region during the first 4 sweeps (Figure S13). Between sweeps 1 and 3, this results in a positive shift in onset potential by 100 mV and a 2 mA/cm$^2$ gain in mass transport limited-current density. This oxidation peak shrinks after 4 sweeps, indicating that further oxidation of the catalyst was limited. This coincided with a loss of activity, with current density decreasing to zero over the subsequent 4 sweeps. We therefore hypothesize that the active surface is a partially oxidized nitride and that the activity is suppressed, as the oxidation progresses, through decreased conductivity and dissolution. This reveals the sensitivity of the catalyst to open circuit potential and oxidizing potentials; durability could be improved by maintaining the catalyst at reducing currents.

## Characterization After Electrochemical Testing

To better understand chemical stability and investigate the mechanisms of failure in acid and base, the films were characterized after activity (CV) and stability (CA) testing using SEM and XPS. After the 10 h CA in acid (Figure 5A), SEM shows that the surface structure had changed completely, with most of the material gone. This structural change likely contributes to the loss in performance over time. After the 40 h CA in base (Figure 5B,C), the structure is distinct from the as-prepared catalyst. The surface was covered with rod-shaped structures, loosely packed into clusters approximately 0.1 μm$^2$ in area, and large cracks (approximately 300 nm across) appeared in the film. We hypothesize

that these cracks may have undercut the film, disturbing its electrical connectivity and performance.

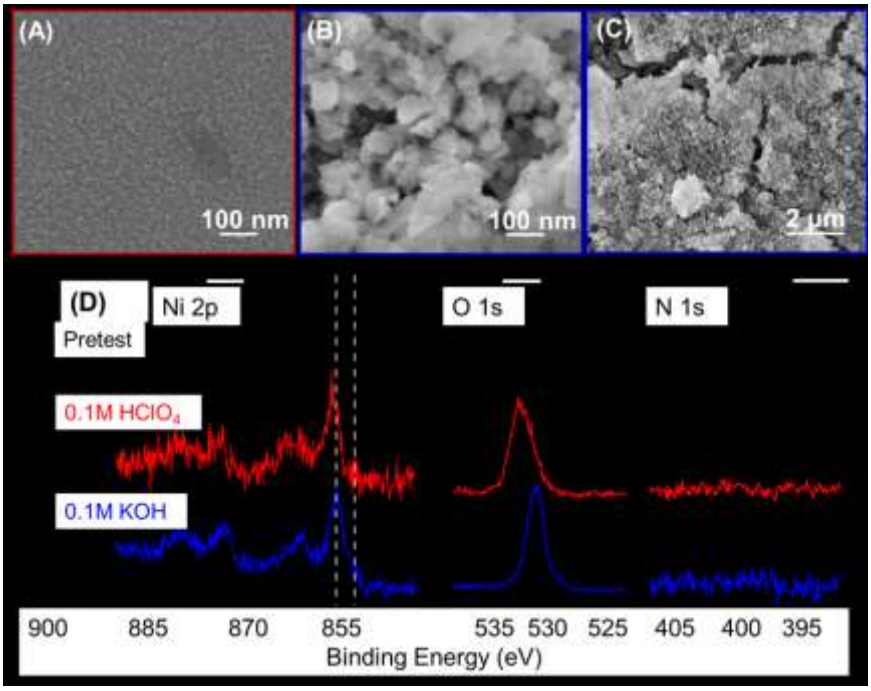


**Figure 5.** Top down SEM images of the nickel nitride films after (A) stability test in acid, and (B, C) stability test in base. (D) High-resolution XPS spectra for as-prepared (black), post-stability acid (red), and post-stability base (blue) for Ni 2p, O 1s, and N 1s regions. Dashed lines are intended as guides for the reader.

The XPS spectra (Figure 5D) also show a change in elemental composition. Before continuing with this discussion, it is necessary to note that accurate quantitative analysis of this XPS data is difficult due to the complexity of the Ni 2p spectrum, so all statements of composition are meant as best approximation. Elemental quantification of the nickel nitride revealed a ratio of Ni to N of approximately 3.5, consistent with a mixture of $Ni_3N$ and $Ni_4N$ observed in XRD. Prior to testing, peaks were identified in the Ni $2p_{3/2}$ region at binding energies of 853.0 and 855.2 eV (dashed lines), corresponding to the interstitial nitride ($Ni^{\delta+}$, $\delta$ = 0-2) and oxide ($Ni^{2+}$), respectively. There are satellite peaks in the region 860 – 865 eV. This matches well with literature spectra for nickel nitride.[58] In the O 1s region, the low energy peak at 529.3 eV corresponds to the nickel oxide, while we associate the higher energy peak with hydroxide (literature value of 531.1 eV) and carbonyl species (most likely carbonate, literature value of 532.8 eV).[59] Finally, the N 1s peak at 397.6 eV corresponds to a metal nitride.

After stability testing in acid, the surface composition changed drastically. The Ni $2p_{3/2}$ peaks shifted to higher binding energies, with the largest peak at 855.8 eV, indicating the

$Ni^{2+}$ oxidation state. The N 1s peak disappeared, corresponding to a loss of nitrogen from the surface. The O 1s peaks increased in intensity relative to the Ni and indicate the presence of hydroxide and carbonate species (from air exposure prior to characterization).[60] In conjunction with the structural changes observed by SEM, this indicates an extensive reorganization of the surface during testing, resulting in a surface that more closely resembles $Ni(OH)_2$ than the original $Ni_4N$.[61] Similar composition changes were observed after CV testing in acid (Figure S14). From XPS it is not possible to determine when these changes occurred, though it seems likely that they were caused by exposure to oxidizing potentials during testing or open circuit potential when the catalyst is removed from electrolyte. These structural and composition changes indicate that overall chemical stability is poor in acid. However, an analysis of potential corrosion current, as well as the poor ORR activity of the underlying Ti and glassy carbon in acid, indicates that the $Ni_xN$ catalyst is responsible for the current observed during the stability test (see SI for details).

The composition change after stability testing in base is similar. The primary remaining Ni $2p_{3/2}$ peak is at 855.9 eV and there is no N 1s signal at the surface, indicating a complete conversion at the surface to a hydroxide structure. The O 1s spectrum shows a small oxide peak, but hydroxide is the dominant species. Comparatively, the composition changes after CV testing are minor, with nitride composition retained (Fig. S14). This was confirmed by the bulk NEXAFS spectra, which showed no significant change between this and the as-deposited sample (Fig. S15). This electrochemical, microscopic, and spectroscopic investigation of stability and failure mechanisms has revealed that activity loss is correlated with the conversion of the nitride to hydroxide and associated material property changes. Due to the sensitivity of the activity and stability of these catalysts to applied potential, future work should focus on probing the stability of these catalysts as a function of applied potential. We hypothesize that stability would be more challenging at more oxidizing conditions, since extensive catalyst oxidation was found to detrimentally impact activity and stability.

To gain insight into oxide phases observed experimentally, we evaluated the stability of oxide phases in the presence of $Ni_3N$ and $Ni_4N$ with DFT. The optimized bulk structures of $Ni_3N$ and $Ni_4N$ are in good agreement with the XRD and SADP results, as well as previously reported bulk parameters (a=b=4.619 and c=4.307 Å for $Ni_3N$, a=b=c=3.730 Å for $Ni_4N$).[62,63] We modeled $\sqrt{3} \times \sqrt{3}$ structures for $Ni_3N$ (0001) and $Ni_4N$ (111) to minimize the lattice mismatch between nickel nitrides ($Ni_3N$ and $Ni_4N$) and nickel oxides (NiOOH and NiO). In the next step we simulated monolayer films of NiOOH and NiO supported on $Ni_3N$ and $Ni_4N$ (Figure 6A). We considered all possible adsorption sites and surface termination to minimize the oxide nitride interface formation energy. The formation energies of nickel oxides films (NiOOH and NiO) on nickel nitrides ($Ni_3N$ and $Ni_4N$) are calculated as following:

$$E_{Formation} = \left[E_{slab,oxide+nitride} - E_{slab,nitride} - nE_{bulk,oxide}\right]/n,$$

Where $E_{slab,oxide+nitride}$, $E_{slab,nitride}$ and $E_{bulk,nitride}$ are electronic energies of the total system, slab structure of nitrides and bulk nickel oxides. The *n* is the number of oxide units in the total system. The most stable geometries for NiOOH and NiO on $Ni_3N$ and $Ni_4N$ are shown in Figure 6A and Table 1 summarizes the results of formation energy calculations. These results show that NiOOH layer is effectively stabilized by -0.67 and -0.53 eV/f.u on $Ni_3N$ and $Ni_4N$, respectively, while NiO is significantly destabilized.

**Table 1.** The calculated formation energy of Ni oxide species on Ni nitrides.

| Formation energy (eV/f.u.) | $Ni_3N$ | $Ni_4N$ |
|---|---|---|
| NiOOH | -0.67 | -0.53 |
| NiO | 1.60 | 1.64 |

To further elaborate the formation of different oxide phases during ORR testing, as well as differences in stability between acid and alkaline electrolyte, we constructed Pourbaix diagrams. Figure 6 shows (A) the most stable geometries of the NiO and NiOOH overlayers as well as the theoretically calculated Pourbaix diagrams for (B) bulk Ni, (C) $Ni_3N$, and (D) $Ni_4N$. The region of interest for ORR is 0.2 $V_{RHE}$ to 1.23 $V_{RHE}$, below the upper dashed line in the Pourbaix diagram. The strong formation energy of NiOOH on both $Ni_3N$ and $Ni_4N$ results in the expansion of NiOOH area in the Pourbaix diagrams (Fig 6C and D). Hence, the observed oxidized phase in the experiment can be attributed to the stabilized NiOOH on the nickel nitride surfaces, particularly in alkaline electrolyte. This analysis also shows that nickel nitride surfaces are not stable under acidic environment due to dissolution of $Ni^{2+}$ ions. Differences in surface composition and coverage between these electrolytes may contribute to the observed differences in ORR activity and selectivity.

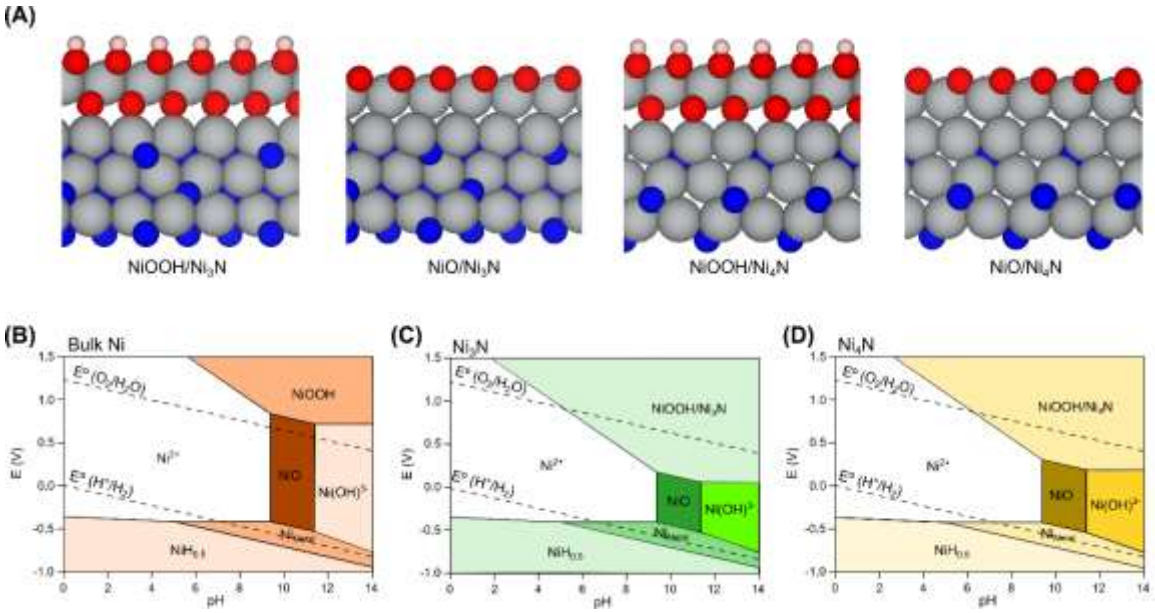


**Figure 6.** (A) Optimized geometries of NiO and NiOOH supported on $Ni_3N$ and $Ni_4N$, respectively. Pourbaix diagrams of (B) bulk Ni, (C) $Ni_3N$, and (D) $Ni_4N$. (B) is based on the experimental values of formation free energies of bulk phases[62,63], and the stabilization energies of nickel nitrides on NiOOH were added to construct (C) and (D). NiO is destabilized on the nickel nitrides, thus the bulk formation free energy was used. Color codes: silver (Ni), blue (N), red (O), pink (H). The equilibrium potentials of $O_2/H_2O$ (1.23 $V_{RHE}$) and $H^+/H_2$ (0.00 $V_{RHE}$) are marked with dashed lines.

The above theoretical investigation provides a basic understanding of the formation of possible nickel oxide phases on the examined nickel nitrides, which is of particular interest due to recent DFT calculations showing that the formation of an oxide over-layer on cobalt nitride promotes ORR.[64] This is in agreement with our experimental observation of extensive surface oxidation after ORR testing. While the XPS and NEXAFS results indicate a surface hydroxide species, these are *ex situ* measurements, taken after the catalysts had been exposed to air, and thus cannot be used to determine the surface composition under reaction conditions. This will be the subject of future investigations utilizing operando spectroscopies.

It is important to note that the Pourbaix diagram is based on thermodynamics and does not provide any information about the kinetics of the phase transition. Thus, while the nickel nitride is not predicted to be stable in acid, several hours of stability were achieved, perhaps because the oxidation or dissolution processes are slow kinetically. This can serve as a design principle for further catalyst development. Superior stability is observed in base, where the catalyst is more thermodynamically stable.

The use of a well-defined and carbon-free catalyst morphology facilitated a combined experiment-theory approach to determining the active surface of the catalyst. With the

insights into the origins of activity and stability obtained through the study of this model system, efforts to improve this catalyst fall into two main categories.[65] First, intrinsic activity and stability can be improved through alloying with a more stable transition metal nitride, which has been demonstrated for several nitride systems.[22,23,29] Based on the Pourbaix calculations and the potential of activation via oxide over-layer formation,[64] a promising candidate would be a metal nitride which forms a stable, passivating oxide or hydroxide surface in acid and alkaline electrolyte. Second, after discovery of a promising material system, the number of active sites can be increased through nanostructuring and supporting the catalyst on a high surface area material such as N-doped carbon.[54,55]

## Conclusions

In summary, nickel nitride thin films were found to be active ORR catalysts, achieving activity comparable to the metal nitrides reported in the literature. Reactive sputtering is highlighted as a promising route to synthesize transition metal nitride electrocatalysts with a variety of compositions and crystal structures, allowing for fundamental investigation of the active surface. By synthesizing the catalyst in a carbon-free morphology, we were able to use a combined experiment-theory approach to isolate the activity of the nickel nitride and found that it is an active and reasonably stable non-precious metal catalyst for ORR in acid, as well as in base. In future work, catalyst activity and stability could be improved through alloying and nanostructuring. *Ex situ* XAS and XPS characterization indicated that an oxide overlayer readily forms on the catalyst surface. DFT calculations predicted similar surface oxidation under reaction conditions, which was shown to correlate with changes in electrochemical activity and stability. This surface oxidation can serve as a design principle for a variety of metal nitride catalysts and demonstrates the importance of complementary experimental and theoretical studies.

## Associated Content

Supporting Information available**:** Supplementary experimental characterization (TEM, XRD, NEXAFS, electrochemistry, and XPS), and details for $H_2O_2$ selectivity, Tafel, and TOF calculations. Raw data from all main text figures are also provided, in line with the U.S. Department of Energy requirements.

## Author Information & Notes

Corresponding Authors:
*Email: lking10@stanford.edu
*Email: jaramillo@stanford.edu

ORCID
Melissa E. Kreider 0000-0003-1750-6860
Yunzhi Liu 0000-0003-0524-4023
Seoin Back: 0000-0003-4682-0621
Samira Siahrostami: 0000-0002-1192-4634
Dennis Nordlund: 0000-0001-9524-6908
Laurie A. King: 0000-0002-0772-2378
Thomas F. Jaramillo: 0000-0001-9900-0622

Notes

The authors declare no competing financial interest.

## Acknowledgement

The authors gratefully acknowledge the support of the Toyota Research Institute. The US Department of Energy (DoE) Office of Basic Energy Sciences (BES) is gratefully acknowledged for primary support for SUNCAT Center for Interface Science and Catalysis. Part of this work was performed at the Stanford Nano Shared Facilities (SNSF) and the Stanford Nanofabrication Facility (SNF), supported by the National Science Foundation under Award ECCS-1542152. Use of the Stanford Synchrotron Radiation Lightsource, SLAC National Accelerator Laboratory, is supported by the U.S. Department of Energy, Office of Science, Office of Basic Energy Sciences under Contract No. DE-AC02-76SF00515. This research used resources of the National Energy Research Scientific Computing Center (NERSC), a U.S. Department of Energy Office of Science User Facility operated under Contract No. DE-AC02-05CH11231. AG would like to thank J. Vinson at NIST for his support with the OCEAN code.

## References

(1) Ramaswamy, N.; Mukerjee, S. Fundamental Mechanistic Understanding of Electrocatalysis of Oxygen Reduction on Pt and Non-Pt Surfaces: Acid versus Alkaline Media. *Adv. Phys. Chem.* **2012**, *2012*, 1–17.

(2) Gasteiger, H. A.; Kocha, S. S.; Sompalli, B.; Wagner, F. T. Activity Benchmarks and Requirements for Pt, Pt-Alloy, and Non-Pt Oxygen Reduction Catalysts for PEMFCs. *Appl. Catal. B Environ.* **2005**, *56*, 9–35.

(3) Rabis, A.; Rodriguez, P.; Schmidt, T. J. Electrocatalysis for Polymer Electrolyte Fuel Cells : Recent Achievements and Future Challenges. *ACS Catal.* **2012**, *2*, 864–890.

(4) Greeley, J.; Stephens, I. E. L.; Bondarenko, A. S.; Johansson, T. P.; Hansen, H. A.; Jaramillo, T. F.; Rossmeisl, J.; Chorkendorff, I.; Nørskov, J. K. Alloys of

Platinum and Early Transition Metals as Oxygen Reduction Electrocatalysts. *Nat. Chem.* **2009**, *1*, 552–556.

(5) Stamenkovic, V. R.; Fowler, B.; Mun, B. S.; Wang, G.; Ross, P. N.; Lucas, C. A.; Markovic, N. M. Improved Oxygen Reduction Activity on Pt3Ni(111) via Increased Surface Site Availability. *Science* **2007**, *315* (5811), 493–498.

(6) Chen, S.; Sheng, W.; Yabuuchi, N.; Ferreira, P. J.; Allard, L. F. Origin of Oxygen Reduction Reaction Activity on "Pt3Co" Nanoparticles: Atomically Resolved Chemical Compositions and Structures. *J. Phys. Chem. C* **2009**, *113*, 1109–1125.

(7) Zhou, M.; Wang, H.; Elnabawy, A. O.; Hood, Z. D.; Chi, M.; Xiao, P.; Zhang, Y.; Mavrikakis, M.; Xia, Y. Facile One-Pot Synthesis of Pd@Pt 1L Octahedra with Enhanced Activity and Durability toward Oxygen Reduction. *Chem. Mater.* **2019**, *31* (4), 1370–1380.

(8) Jaouen, F.; Proietti, E.; Lefevre, M.; Chenitz, R.; Dodelet, J.-P.; Wu, G.; Chung, H. T.; Johnston, C. M.; Zelenay, P. Recent Advances in Non-Precious Metal Catalysis for Oxygen-Reduction Reaction in Polymer Electrolyte Fuel Cells. *Energy Environ. Sci.* **2011**, *4*, 114–130.

(9) Shinozaki, K.; Zack, J. W.; Richards, R. M.; Pivovar, B. S.; Kocha, S. S. Oxygen Reduction Reaction Measurements on Platinum Electrocatalysts Utilizing Rotating Disk Electrode Technique. *J. Electrochem. Soc.* **2015**, *162* (10), F1144–F1158.

(10) Camara, G. A.; Ticianelli, E. A.; Mukerjee, S.; Lee, S. J.; Mcbreen, J. The CO Poisoning Mechanism of the Hydrogen Oxidation Reaction in Proton Exchange Membrane Fuel Cells. *J. Electrochem. Soc.* **2002**, *149* (6), 748–753.

(11) Suntivich, J.; Gasteiger, H. A.; Yabuuchi, N.; Nakanishi, H.; Goodenough, J. B.; Shao-Horn, Y. Design Principles for Oxygen-Reduction Activity on Perovskite Oxide Catalysts for Fuel Cells and Metal-Air Batteries. *Nat. Chem.* **2011**, *3* (7), 546–550.

(12) Stoerzinger, K. A.; Li, C.; Venkatesan, T.; Shao-Horn, Y. Highly Active Epitaxial La(1−x)SrxMnO3 Surfaces for the Oxygen Reduction Reaction: Role of Charge Transfer. *J. Phys. Chem. Lett.* **2015**, *6*, 1435–1440.

(13) Wei, W.; Liang, H.; Parvez, K.; Zhuang, X.; Feng, X.; Müllen, K. Nitrogen-Doped Carbon Nanosheets with Size-Defined Mesopores as Highly Efficient Metal-Free Catalyst for the Oxygen Reduction Reaction. *Angew. Chemie* **2014**, *126*, 1596–1600.

(14) Ratso, S.; Sahraie, N. R.; Sougrati, M. T.; Kaarik, M.; Kook, M.; Saar, R.; Paiste, P.; Jia, Q.; Leis, J.; Mukerjee, S.; Jaouen, F.; Tammeveski, K. Synthesis of Highly-Active Fe – N – C Catalysts for PEMFC with Carbide-Derived Carbons. *J. Mater. Chem. A* **2018**, *6*, 14663–14674.

(15) Shao, Y.; Sui, J.; Yin, G.; Gao, Y. Nitrogen-Doped Carbon Nanostructures and Their Composites as Catalytic Materials for Proton Exchange Membrane Fuel Cell. *Appl. Catal. B Environ.* **2008**, *79*, 89–99.

(16) Chung, H. T.; Cullen, D. A.; Higgins, D.; Sneed, B. T.; Holby, E. F.; More, K. L.; Zelenay, P. Direct Atomic-Level Insight into the Active Sites of a High-Performance PGM-Free ORR Catalyst. *Science* **2017**, *357*, 479–484.

(17) Dong, S.; Chen, X.; Zhang, X.; Cui, G. Nanostructured Transition Metal Nitrides for Energy Storage and Fuel Cells. *Coord. Chem. Rev.* **2013**, *257* (13–14), 1946–1956.

(18) Oyama, S. T. Preparation and Catalytic Properties of Transition Metal Carbides and Nitrides. *Catal. Today* **1992**, *15* (2), 179–200.

(19) An, L.; Huang, W.; Zhang, N.; Chen, X.; Xia, D. A Novel CoN Electrocatalyst with High Activity and Stability toward Oxygen Reduction Reaction. *J. Mater. Chem. A* **2014**, *2*, 62–65.

(20) Liu, M.; Dong, Y.; Wu, Y.; Feng, H.; Li, J. Titanium Nitride Nanocrystals on Nitrogen-Doped Graphene as an Efficient Electrocatalyst for Oxygen Reduction Reaction. *Chem. - A Eur. J.* **2013**, *19* (44), 14781–14786.

(21) Yang, W.; Rehman, S.; Chu, X.; Hou, Y.; Gao, S. Transition Metal (Fe, Co and Ni) Carbide and Nitride Nanomaterials: Structure, Chemical Synthesis and Applications. *ChemNanoMat* **2015**, *1* (6), 376–398.

(22) Tian, X. L.; Wang, L.; Chi, B.; Xu, Y.; Zaman, S.; Qi, K.; Liu, H.; Liao, S.; Xia, B. Y. Formation of a Tubular Assembly by Ultrathin Ti0.8Co0.2N Nanosheets as Efficient Oxygen Reduction Electrocatalysts for Hydrogen-/Metal-Air Fuel Cells. *ACS Catal.* **2018**, *8*, 8970–8975.

(23) Tian, X.; Luo, J.; Nan, H.; Fu, Z.; Zeng, J.; Liao, S. Binary Transition Metal Nitrides with Enhanced Activity and Durability for the Oxygen Reduction Reaction. *J. Mater. Chem. A* **2015**, *3* (32), 16801–16809.

(24) Vaughn, D. D.; Araujo, J.; Meduri, P.; Callejas, J. F.; Hickner, M. A.; Schaak, R. E. Solution Synthesis of Cu3PdN Nanocrystals as Ternary Metal Nitride Electrocatalysts for the Oxygen Reduction Reaction. *Chem. Mater.* **2014**, *26* (21), 6226–6232.

(25) Ningthoujam, R. S.; Gajbhiye, N. S. Synthesis, Electron Transport Properties of Transition Metal Nitrides and Applications. *Prog. Mater. Sci.* **2015**, *70*, 50–154.

(26) Wang, T.; Yan, Z.; Michel, C.; Pera-Titus, M.; Sautet, P. Trends and Control in the Nitridation of Transition-Metal Surfaces. *ACS Catal.* **2017**, 63–68.

(27) Chen, W.-F.; Muckerman, J. T.; Fujita, E. Recent Developments in Transition Metal Carbides and Nitrides as Hydrogen Evolution Electrocatalysts. *Chem. Commun.* **2013**, *49* (79), 8896–8909.

(28) Sun, T.; Wu, Q.; Che, R.; Bu, Y.; Jiang, Y.; Li, Y.; Yang, L.; Wang, X.; Hu, Z. Alloyed Co-Mo Nitride as High-Performance Electrocatalyst for Oxygen Reduction in Acidic Medium. *ACS Catal.* **2015**, *5* (3), 1857–1862.

(29) Cao, B.; Neuefeind, J. C.; Adzic, R. R.; Khalifah, P. G. Molybdenum Nitrides as

Oxygen Reduction Reaction Catalysts: Structural and Electrochemical Studies. *Inorg. Chem.* **2015**, *54* (5), 2128–2136.

(30) Huang, Q.; Chen, S.; Ma, T.; Zou, H.; Yang, W. TiN Supported Cobalt and Molybdenum Nitrides as an Efficient Oxygen Reduction Reaction Catalyst in Acid Medium. *Int. J. Electrochem. Sci.* **2017**, *12* (7), 6340–6351.

(31) Shalom, M.; Ressnig, D.; Yang, X.; Clavel, G.; Fellinger, T. P.; Antonietti, M. Nickel Nitride as an Efficient Electrocatalyst for Water Splitting. *J. Mater. Chem. A* **2015**, *3* (15), 8171–8177.

(32) Fan, Y.; Ida, S.; Staykov, A.; Akbay, T.; Hagiwara, H.; Matsuda, J.; Kaneko, K.; Ishihara, T. Ni-Fe Nitride Nanoplates on Nitrogen-Doped Graphene as a Synergistic Catalyst for Reversible Oxygen Evolution Reaction and Rechargeable Zn-Air Battery. *Small* **2017**, *13* (25), 1–8.

(33) Fu, G.; Cui, Z.; Chen, Y.; Xu, L.; Tang, Y.; Goodenough, J. B. Hierarchically Mesoporous Nickel-Iron Nitride as a Cost-Efficient and Highly Durable Electrocatalyst for Zn-Air Battery. *Nano Energy* **2017**, *39* (June), 77–85.

(34) Cui, Z.; Fu, G.; Li, Y.; Goodenough, J. B. Ni3FeN-Supported Fe3Pt Intermetallic Nanoalloy as a High-Performance Bifunctional Catalyst for Metal–Air Batteries. *Angew. Chemie - Int. Ed.* **2017**, *56* (33), 9901–9905.

(35) Zhang, H.; Liu, M.; Cheng, W.; Li, Y.; Zhou, W.; Su, H.; Zhao, X.; Yao, P.; Liu, Q. Metallic Ni3N Quantum Dots as Synergistic Promoter for NiO Nanosheet towards Efficient Oxygen Reduction Electrocatalysis. *J. Phys. Chem. C* **2019**, *123* (14), 8633–8639.

(36) Bravman, J. C.; Sinclair, R. The Preparation of Cross-Section Specimens for Transmission Electron Microscopy. *J. Electron Microsc. Tech.* **1984**, *1*, 53–61.

(37) Gilmore, K.; Vinson, J.; Shirley, E. L.; Prendergast, D.; Pemmaraju, C. D.; Kas, J. J.; Vila, F. D.; Rehr, J. J. Efficient Implementation of Core-Excitation Bethe Salpeter Equation Calculations. *Comput. Phys. Commun.* **2015**, *197*, 109–117.

(38) Vinson, J.; Rehr, J. J.; Kas, J. J.; Shirley, E. L. Bethe-Salpeter Equation Calculations of Core Excitation Spectra. *Phys. Rev. B - Condens. Matter Mater. Phys.* **2011**, *83* (11), 115106.

(39) Rehr, J. J.; Kas, J. J.; Vila, F. D.; Prange, M. P.; Jorissen, K. Parameter-Free Calculations of X-Ray Spectra with FEFF9. *Phys. Chem. Chem. Phys.* **2010**, *12* (21), 5503–5513.

(40) Joubert, D. From Ultrasoft Pseudopotentials to the Projector Augmented-Wave Method. *Phys. Rev. B - Condens. Matter Mater. Phys.* **1999**, *59* (3), 1758–1775.

(41) Kresse, G.; Furthmüller, J. Efficiency of Ab-Initio Total Energy Calculations for Metals and Semiconductors Using a Plane-Wave Basis Set. *Comput. Mater. Sci.* **1996**, *6*, 15–50.

(42) Hammer, B.; Hansen, L. B.; Nørskov, J. K. Improved Adsorption Energetics within

Density-Functional Theory Using Revised Perdew-Burke-Ernzerhof Functionals. *Phys. Rev. B - Condens. Matter Mater. Phys.* **1999**, *59* (11), 7413–7421.

(43) Blöchl, P. E. Projector Augmented-Wave Method. *Phys. Rev. B* **1994**, *50* (24), 17953–17979.

(44) Dudarev, S.; Botton, G. Electron-Energy-Loss Spectra and the Structural Stability of Nickel Oxide: An LSDA+U Study. *Phys. Rev. B - Condens. Matter Mater. Phys.* **1998**, *57* (3), 1505–1509.

(45) Wang, L.; Maxisch, T.; Ceder, G. Oxidation Energies of Transition Metal Oxides within the GGA+U Framework. *Phys. Rev. B - Condens. Matter Mater. Phys.* **2006**, *73*, 195107.

(46) Jain, A.; Hautier, G.; Ong, S. P.; Moore, C. J.; Fischer, C. C.; Persson, K. A.; Ceder, G. Formation Enthalpies by Mixing GGA and GGA + U Calculations. *Phys. Rev. B - Condens. Matter Mater. Phys.* **2011**, *84* (4), 1–10.

(47) Fioretti, A. N.; Schwartz, C. P.; Vinson, J.; Nordlund, D.; Prendergast, D.; Tamboli, A. C.; Caskey, C. M.; Tuomisto, F.; Linez, F.; Christensen, S. T.; Toberer E.S.; Lany, S.; Zakutayev, A. Understanding and Control of Bipolar Doping in Copper Nitride. *J. Appl. Phys.* **2016**, *119* (18), 181508.

(48) Esaka, F.; Furuya, K.; Shimada, H.; Imamura, M.; Matsubayashi, N.; Sato, H.; Nishijima, A.; Kawana, A.; Ichimura, H.; Kikuchi, T. Comparison of Surface Oxidation of Titanium Nitride and Chromium Nitride Films Studied by X-Ray Absorption and Photoelectron Spectroscopy. *J. Vac. Sci. Technol. A Vacuum, Surfaces, Film.* **1997**, *15* (5), 2521–2528.

(49) Chen, J. G.; Fischer, D. A.; Hardenbergh, J. H.; Hall, R. B. A Fluorescence-Yield near-Edge Spectroscopy (FYNES) Investigation of the Reaction Kinetics of NiO/Ni(100) with Hydrogen. *Surf. Sci.* **1992**, *279* (1–2), 13–22.

(50) Jackson, A.; Strickler, A.; Higgins, D.; Jaramillo, T. F. Engineering Ru @ Pt Core-Shell Catalysts for Enhanced Electrochemical Oxygen Reduction Mass Activity and Stability. *Nanomaterials* **2018**, *8*, 38–52.

(51) Luo, J.; Tian, X.; Zeng, J.; Li, Y.; Song, H.; Liao, S. Limitations and Improvement Strategies for Early-Transition-Metal Nitrides as Competitive Catalysts toward the Oxygen Reduction Reaction. *ACS Catal.* **2016**, *6*, 6165–6174.

(52) Ando, T.; Izhar, S.; Tominaga, H.; Nagai, M. Ammonia-Treated Carbon-Supported Cobalt Tungsten as Fuel Cell Cathode Catalyst. *Electrochim. Acta* **2010**, *55*, 2614–2621.

(53) Tang, H.; Tian, X.; Luo, J.; Zeng, J.; Li, Y. A Co-Doped Porous Niobium Nitride Nanogrid as an Effective Oxygen Reduction Catalyst. *J. Mater. Chem. A* **2017**, *5*, 14278–14285.

(54) Liu, Y.; Jiang, H.; Zhu, Y.; Yang, X.; Li, C. Transition Metals (Fe, Co, and Ni) Encapsulated in Nitrogen-Doped Carbon Nanotubes as Bi-Functional Catalysts for Oxygen Electrode Reactions. *J. Mater. Chem. A* **2016**, *4* (5), 1694–1701.

(55) Chen, T.; Guo, S.; Yang, J.; Xu, Y.; Sun, J.; Wei, D.; Chen, Z.; Zhao, B.; Ding, W. Nitrogen-Doped Carbon Activated in Situ by Embedded Nickel through the Mott–Schottky Effect for the Oxygen Reduction Reaction. *ChemPhysChem* **2017**, *18* (23), 3454–3461.

(56) Shinagawa, T.; Garcia-Esparza, A. T.; Takanabe, K. Insight on Tafel Slopes from a Microkinetic Analysis of Aqueous Electrocatalysis for Energy Conversion. *Sci. Rep.* **2015**, *5*, 13801–13821.

(57) Yan, B.; Krishnamurthy, D.; Hendon, C. H.; Yan, B.; Krishnamurthy, D.; Hendon, C. H.; Deshpande, S. Surface Restructuring of Nickel Sulfide Generates Optimally Coordinated Active Sites for Oxygen Reduction Catalysis Surface Restructuring of Nickel Sulfide Generates Optimally Coordinated Active Sites for Oxygen Reduction Catalysis. *Joule* **2017**, *1*, 600–612.

(58) Soo Kang, J.; Park, M. A.; Kim, J. Y.; Ha Park, S.; Young Chung, D.; Yu, S. H.; Kim, J.; Park, J.; Choi, J. W.; Jae Lee, K.; Jeong, J.; Jae Ko, M.; Ahn, K-S.; Sung, Y-E. Reactively Sputtered Nickel Nitride as Electrocatalytic Counter Electrode for Dye- and Quantum Dot-Sensitized Solar Cells. *Sci. Rep.* **2015**, *5*, 10450–10460.

(59) Biesinger, M. C.; Payne, B. P.; Lau, L. W. M.; Gerson, A.; Smart, R. S. C. X-Ray Photoelectron Spectroscopic Chemical State Quantification of Mixed Nickel Metal, Oxide and Hydroxide Systems. *Surf. Interface Anal.* **2009**, *41* (4), 324–332.

(60) Weidler, N.; Schuch, J.; Knaus, F.; Stenner, P.; Hoch, S.; Maljusch, A.; Schäfer, R.; Kaiser, B.; Jaegermann, W. X-Ray Photoelectron Spectroscopic Investigation of Plasma- Enhanced Chemical Vapor Deposited NiOx, NiOx(OH)y, and CoNiOx(OH)y: Influence of the Chemical Composition on the Catalytic Activity for the Oxygen Evolution Reaction. *J. Phys. Chem. C* **2017**, *121*, 6455–6463.

(61) Grosvenor, A. P.; Biesinger, M. C.; Smart, R. S. C.; McIntyre, N. S. New Interpretations of XPS Spectra of Nickel Metal and Oxides. *Surf. Sci.* **2006**, *600* (9), 1771–1779.

(62) Leineweber, A.; Jacobs, H.; Hull, S. Ordering of Nitrogen in Nickel Nitride Ni3N Determined by Neutron Diffraction. *Inorg. Chem.* **2001**, *40* (23), 5818–5822.

(63) Nagakura, S.; Ōtsuka, N.; Hirotsu, Y. Electron State of Ni4N Studied by Electron Diffraction. *J. Phys. Soc. Japan* **1973**, *35* (5), 1492–1495.

(64) Abroshan, H.; Bothra, P.; Back, S.; Kulkarni, A. R.; Norskov, J. K.; Siahrostami, S. An Ultra-Thin Cobalt-Oxide Overlayer Promotes Catalytic Activity of Cobalt Nitride for Oxygen Reduction Reaction. *J. Phys. Chem. C* **2018**, *122* (9), 4783–4791.

(65) Seh, Z. W.; Kibsgaard, J.; Dickens, C. F.; Chorkendorff, I.; Nørskov, J. K.; Jaramillo, T. F. Combining Theory and Experiment in Electrocatalysis: Insights into Materials Design. *Science* **2017**, *355* (6321).

**TOC image**: